Magnetic ordering of the buckled honeycomb lattice antiferromagnet Ba_2NiTeO_6

Shinichiro Asai,[1] Minoru Soda,[1] Kazuhiro Kasatani,[2] Toshio Ono,[2] Maxim Avdeev,[3] and Takatsugu Masuda[1]

[1]*Institute for Solid State Physics, The University of Tokyo, Kashiwanoha, Kashiwa, Chiba 277-8581, Japan*
[2]*Department of Physical Science, Osaka Prefecture University, Sakai, Osaka 599-8531, Japan*
[3]*Bragg Institute, Australian Nuclear Science and Technology Organization, Lucas Heights, New South Wales 2234, Australia*

We investigate the magnetic order of the buckled honeycomb lattice antiferromagnet Ba_2NiTeO_6 and its related antiferromagnet $Ba_3NiTa_2O_9$ by neutron diffraction measurements. We observe magnetic Bragg peaks below the transition temperatures, and identify propagation vectors for these oxides. A combination of representation analysis and Rietveld refinement leads to a collinear magnetic order for Ba_2NiTeO_6 and a $120°$ structure for $Ba_3NiTa_2O_9$. We find that the spin model of the bilayer triangular lattice is equivalent to that of the two-dimensional *buckled honeycomb lattice* having magnetic frustration. We discuss the magnetic interactions and single-ion anisotropy of Ni^{2+} ions for Ba_2NiTeO_6 in order to clarify the origin of the collinear magnetic structures. Our calculation suggests that the collinear magnetic order of Ba_2NiTeO_6 is induced by the magnetic frustration and easy-axis anisotropy.

I. INTRODUCTION

Triangular lattice antiferromagnets have been extensively studied by many researchers since Anderson proposed the resonating valence-bond state [1]. A $120°$ structure is the ground state for the two-dimensional (2D) Heisenberg triangular lattice antiferromagnet, which has been reported in a number of materials, including $LiCrO_2$ [2], $Rb_4Mn(MoO_4)_3$ [3], and $Ba_3NiNb_2O_9$ [4]. On the other hand, a neutron scattering study has suggested a two-dimensional magnetic correlation and no three-dimensional magnetic order down to 2 K for $NaCrO_2$ and $KCrO_2$ [5]. Additional terms arising from further-neighbor magnetic interactions and anisotropy induce various types of magnetic order and phase diagrams [6]. In $CsCoCl_3$, the ferrimagnetic order and partially disordered state appear as the ground state and thermally induced state, respectively, owing to the Ising spins of Co^{2+} ions [7]. The four-sublattice collinear antiferromagnetic order in $CuFeO_2$ is stabilized by a strong third-neighbor interaction [8]. The amplitude-modulated antiferromagnetic order induced by the Ruderman-Kittel-Kasuya-Yosida (RKKY)-type interlayer interaction is reported in the metallic triangular antiferromagnet Ag_2NiO_2 [9]. In the case of $S = 1/2$ spins, a combination of quantum fluctuation and higher-order perturbative terms suppresses the conventional ordering of spins, and induces an exotic ground state, such as the spin liquid state in $(BEDT-TTF)_2Cu_2(CN)_3$ [10] and the condensed valence-bond state in $LiZn_2Mo_3O_8$ [11]. The ground state of a triangular lattice antiferromagnet is thus sensitive to additional terms, and therefore the search for a novel framework based on a triangular lattice is a good strategy for the discovery of a nontrivial state.

In Ba_2NiTeO_6, a pair of triangular lattices of Ni^{2+} ions ($S = 1$) are coupled through face-shared TeO_6 octahedra, and form a bilayer triangular lattice, as shown in Fig. 1(a) [12]. Copies of the bilayer triangular lattice are produced by R-centering translation. In this paper, we define $J_n^{(Te)}$ as the nth-neighbor interaction in Ba_2NiTeO_6. The pathways of the interactions $J_n^{(Te)}$ are shown in Fig. 1(b). The distances between a Ni^{2+} ion and the first-, second-, and third-neighbor Ni^{2+} ions are comparable, which means that this compound

is not a conventional two-dimensional triangular lattice antiferromagnet because of its unique interlayer coupling. So far $Ba_3Mn_2O_8$ is known to have similar bilayer triangular lattices of Mn^{5+} ions ($S = 1$) [13]. The competition between magnetic interactions is, however, weak for $Ba_3Mn_2O_8$ because of the strong coupling corresponding to $J_2^{(Te)}$ in Fig. 1(a), which leads to the formation of singlet dimers at low temperatures [14]. The inelastic neutron scattering measurements for $Ba_3Mn_2O_8$ suggest that the competition between the interdimer interactions enhances the quasi-two-dimensional behavior of the bilayer triangular lattice [15]. In the case of Ba_2NiTeO_6, the dimerization of Ni^{2+} ions is disturbed because Ni^{2+} ions are well separated by TeO_6 octahedra, and, instead, triangular lattices coupled by the interaction $J_1^{(Te)}$ form a *buckled honeycomb lattice,* as shown in Figs. 1(c) and 1(d), that would induce nontrivial magnetic order. Indeed, the magnetic susceptibility and heat capacity measurements for this compound identified a magnetic transition at 8.6 K, and a large value of the frustration parameter $\theta_W/T_N = 18.6$, where θ_W is the Weiss temperature and T_N is the magnetic transition temperature [16].

For comparison, we focus on $Ba_3NiTa_2O_9$ as a reference for quasi-two-dimensional triangular lattice antiferromagnets. $Ba_3NiTa_2O_9$ includes a triangular lattice of Ni^{2+} ions separated by two nonmagnetic layers of TaO_6 octahedra, as shown in Fig. 1(e) [17]. We define $J_n^{(Ta)}$ as the nth-neighbor interaction in $Ba_3NiTa_2O_9$, whose pathways are shown in Fig. 1(f). This compound is a good candidate for a reference compound of Ba_2NiTeO_6 because they have similar magnetic NiO_6 layers. It is the isostructural material of $Ba_3NiNb_2O_9$ [4] which indicates that the behavior of a quasi-two-dimensional triangular lattice is expected for $Ba_3NiTa_2O_9$. The magnetic transition at 3.2 K was identified by magnetic susceptibility and heat capacity measurements [18].

In this paper, we investigate the magnetic order of the buckled honeycomb lattice antiferromagnet Ba_2NiTeO_6 and its related compound $Ba_3NiTa_2O_9$ by using powder neutron diffraction measurements. Magnetic Bragg peaks were observed below the transition temperatures for these oxides. The magnetic structures were determined as being a collinear
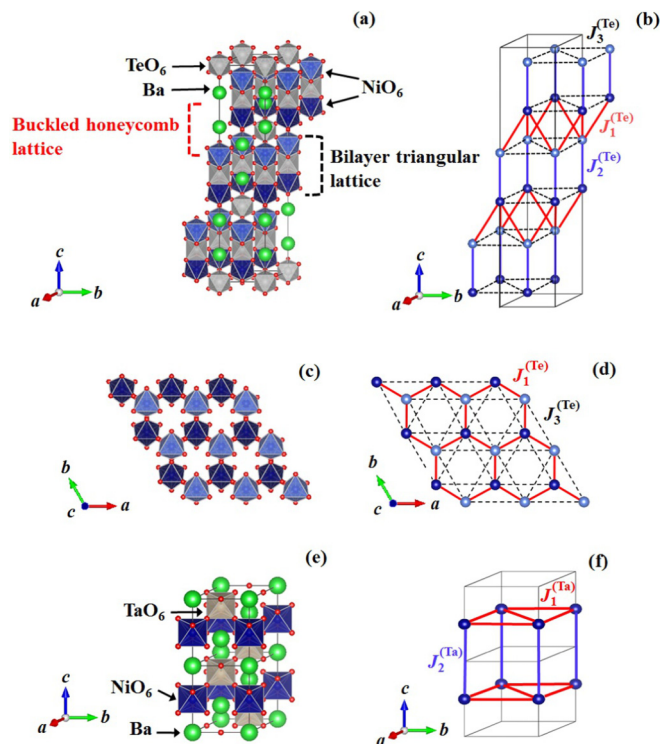
FIG. 1. (a) Crystal structure of Ba_2NiTeO_6. (b) Pathways of the interactions $J_n^{(Te)}$ in Ba_2NiTeO_6. The red and blue solid lines represent $J_1^{(Te)}$ and $J_2^{(Te)}$, respectively. The black dotted lines represent $J_3^{(Te)}$. The light and dark blue spheres represent the Ni^{2+} ions. (c) Arrangement of NiO_6 octahedra in two triangular lattices coupled by the interaction $J_1^{(Te)}$ for Ba_2NiTeO_6. (d) Arrangement of Ni^{2+} ions in two triangular lattices coupled by the interaction $J_1^{(Te)}$ for Ba_2NiTeO_6. (e) Crystal structure of $Ba_3NiTa_2O_9$. (f) Pathways of the interactions $J_n^{(Ta)}$ in $Ba_3NiTa_2O_9$. The red and blue solid lines represent $J_1^{(Ta)}$ and $J_2^{(Ta)}$, respectively. The blue spheres represent the Ni^{2+} ions.

magnetic order for Ba_2NiTeO_6 and a $120°$ structure for $Ba_3NiTa_2O_9$ by using representation analyses and Rietveld refinement. A comparison of the crystal structure between these two compounds reveals that magnetic anisotropy and interlayer interactions are the origins of the difference in the magnetic structure. In order to clarify the origin of collinear order for Ba_2NiTeO_6, we investigate the ground state of the bilayer triangular lattice, which is in fact equivalent to a *buckled honeycomb lattice*, having classical Heisenberg spins with easy-axis anisotropy.

II. EXPERIMENTS

The polycrystalline samples Ba_2NiTeO_6 and $Ba_3NiTa_2O_9$ were synthesized by the solid state reaction [18]. Powder neutron scattering measurements were performed at the high resolution powder diffractometer ECHIDNA at OPAL reactor, ANSTO. The wavelength λ of 2.4395 Å was obtained by a Ge 331 monochromator. A $5'$ collimator was placed in front of the sample. Temperature control was achieved by the Orange cryostat. The obtained patterns were analyzed by the Rietveld method using the FULLPROF software [19]. Candidates for the magnetic structure compatible with the lattice symmetry were
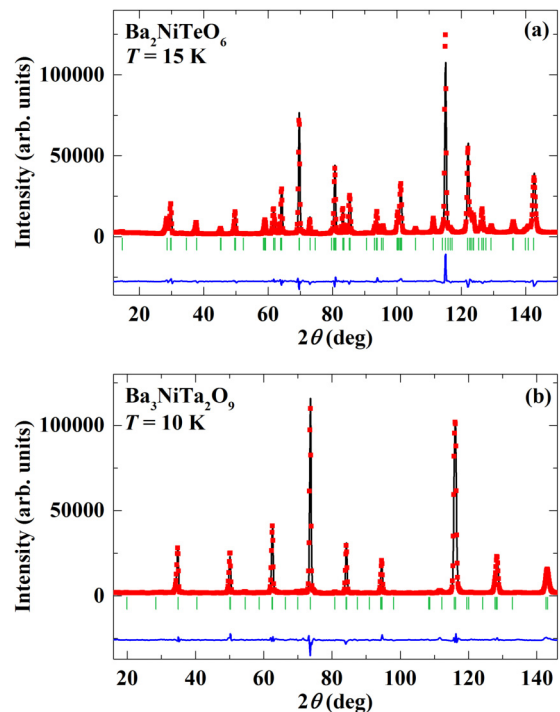

FIG. 2. Neutron diffraction patterns for (a) Ba_2NiTeO_6 at 15 K and (b) $Ba_3NiTa_2O_9$ at 10 K. The solid squares and solid line above the vertical bars show the obtained and calculated data, respectively. The vertical bars show the positions of the Bragg peaks. The solid line below the bars shows the difference curve.

obtained by the SARA*h* software [20]. We used the VESTA software [21] for drawing the crystal and magnetic structures.

III. RESULTS AND ANALYSIS

Figures 2(a) and 2(b) show the neutron diffraction patterns for Ba_2NiTeO_6 at 15 K and $Ba_3NiTa_2O_9$ at 10 K, respectively. These profiles can be fit with a hexagonal structure with the space group $R\bar{3}m$ for Ba_2NiTeO_6 and $P\bar{3}m$ for $Ba_3NiTa_2O_9$. The lattice parameters $a = 5.7839(1)$ and $c = 28.5401(2)$ Å are evaluated for Ba_2NiTeO_6. The structural parameters obtained by a structure analysis with the profile factors ($R_{wp} = 9.82\%$, $R_e = 1.99\%$) are listed in Table I, which is consistent with a previous report [12]. The evaluated bond lengths and bond angles of the NiO_6 octahedron for Ba_2NiTeO_6 are listed in Table II, which means that the NiO_6 octahedron of Ba_2NiTeO_6 is strongly distorted. This distortion may be due

TABLE I. Structural parameters of Ba_2NiTeO_6 at 15 K.

Atom	Site	x	y	z
Ba1	$6c$	0	0	0.1257(2)
Ba2	$6c$	0	0	0.2840(2)
Ni	$6c$	0	0	0.4064(1)
Te1	$3a$	0	0	0
Te2	$3b$	0	0	0.5
O1	$18h$	0.1508(2)	0.8492(2)	0.4589(1)
O2	$18h$	0.1771(3)	0.8229(3)	0.6277(1)

TABLE II. Evaluated bond lengths and bond angles of the NiO_6 octahedron for Ba_2NiTeO_6.

Bond length (Å)		Bond angle (deg)	
Ni-O1 $\times$ 3	2.127(3)	O1-Ni-O1 $\times$ 3	75.93(12)
Ni-O2 $\times$ 3	2.024(2)	O2-Ni-O2 $\times$ 3	98.77(15)
		O1-Ni-O2 $\times$ 6	91.58(15)
		O1-Ni-O2 $\times$ 3	164.04(18)

to the difference in the effective ionic radius between the Ni^{2+} and Te^{6+} ions [22], which induces the mismatch between the NiO_6 octahedra and face-shared TeO_6 octahedra. The lattice parameters $a = 5.7468(1)$ and $c = 7.0604(1)$ Å are obtained for $Ba_3NiTa_2O_9$. The high profile factors ($R_{wp} = 11.0\%$, $R_e = 2.22\%$) are due to the unidentified impurity phase, as observed in Fig. 4(b). The obtained structural parameters listed in Table III are consistent with a previous report [17]. The bond lengths and bond angles of the NiO_6 octahedron evaluated from the structural parameters in Table III are listed in Table IV, which means that the NiO_6 octahedron of $Ba_3NiTa_2O_9$ is almost free of distortion.

The neutron diffraction patterns for Ba_2NiTeO_6 at 3, 6, 8, 9, 10, 12, and 15 K are shown in Fig. 3(a). Below 9 K, three magnetic peaks are observed. The peaks at $15°$, $24°$, and $43°$ are indexed as $(0\,1/2\,1)$, $(0\,1/2\,4)$, and $(0\,3/2\,0)$, respectively. Then, the magnetic propagation vector k_{mag} is identified as $(0,0.5,1)$. The representation analysis with the space group k_{mag} and positions of Ni^{2+} ions for Ba_2NiTeO_6 leads to four irreducible representations. The details of the irreducible representations and the corresponding basis vectors are listed in Table V. In this paper, we assume that the magnetic structure is described by a single irreducible representation. The magnetic structure of Ba_2NiTeO_6 should be then described by one of four basis vectors: (i) ψ_1, (ii) the linear combination of ψ_2 and ψ_3, (iii) the linear combination of ψ_4 and ψ_5, and (iv) ψ_6. We refer to the magnetic structures described by the basis vectors (i)–(iv) as models (i)–(iv), respectively. In order to find the magnetic structure having the best agreement with the experimental result, we carried out a Rietveld analysis with the magnetic models (i)–(iv). The obtained profile at 3 K and fitting results based on the four magnetic models are shown in Fig. 3(b). The obtained magnetic R factors R_{mag} for the magnetic models are listed in the last columns of Table V. We obtained the lowest R_{mag} for model (iii). Thus, we determine that model (iii) is the most appropriate. The determined magnetic structure is shown in Fig. 3(c). Model (iii) allows the spin direction of the Ni^{2+} ion to be

TABLE IV. Evaluated bond lengths and bond angles of the NiO_6 octahedron for $Ba_3NiTa_2O_9$.

Bond length (Å)		Bond angle (deg)	
Ni-O2 $\times$ 6	2.122(5)	O2-Ni-O2 $\times$ 6	88.6(4)
		O2-Ni-O2 $\times$ 3	180.0

perpendicular to the b^* axis. The refinement suggests that there is no component perpendicular to the crystallographic c axis within experimental error and thus the magnetic structure is fully described by the ψ_5 basis vector. The ordered moment for the Ni^{2+} ion of Ba_2NiTeO_6 evaluated by the refinement is shown in Fig. 3(d) as a function of temperature. The ordered moment increases with decreasing temperature below 9 K and amounts to $1.88(6)\mu_B$ at 3 K.

The neutron diffraction patterns for $Ba_3NiTa_2O_9$ at 1.5, 3, 4, 5, and 10 K are shown in Fig. 4(a). Below the transition temperature of 3.2 K, two magnetic peaks are observed. The peaks at $19°$ and $45°$ are indexed as $(1/3\,1/3\,1/2)$ and $(4/3\,1/3\,1/2)$, respectively. Then, the magnetic propagation vector $k_{mag} = (1/3,1/3,1/2)$ is identified. The representation analysis with the space group k_{mag} and positions of Ni^{2+}

TABLE III. Structural parameters of $Ba_3NiTa_2O_9$ at 10 K.

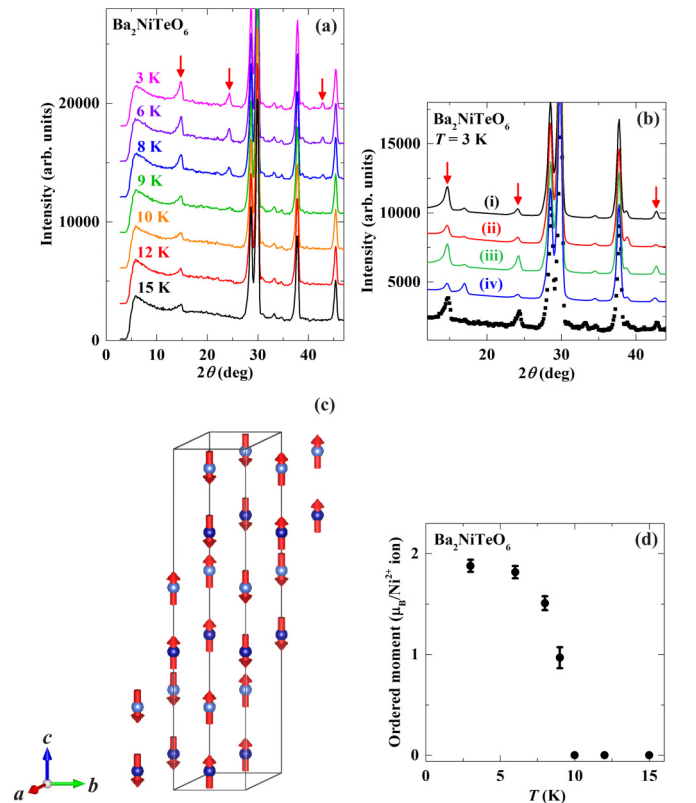| Atom	Site	x	y	z
Ba1	2d	1/3	2/3	0.6619(16)
Ba2	1a	0	0	0
Ni	1b	0	0	0.5
Ta	2d	1/3	2/3	0.1725(12)
O1	4c	0.5	0	0
O2	6i	0.1719(10)	0.3438(10)	0.3223(7)

FIG. 3. (a) Neutron diffraction patterns for Ba_2NiTeO_6 at 3, 6, 8, 9, 10, 12, and 15 K. Data for different temperatures are scaled and vertically offset. The arrows show the magnetic peaks. (b) Neutron diffraction patterns for Ba_2NiTeO_6 at 3 K. The solid squares show the obtained data. The solid lines show fitting results based on the four magnetic models. (c) Determined magnetic structure of Ba_2NiTeO_6. (d) Ordered moment for the Ni^{2+} ion of Ba_2NiTeO_6 as a function of temperature.

TABLE V. Irreducible representations, basis vectors for the space group $R\bar{3}m$ with $\boldsymbol{k}_{\mathrm{mag}} = (0,0.5,1)$, corresponding magnetic model for Rietveld refinement, and magnetic R factors R_{mag}. The coordinates of the Ni(1) and Ni(2) atoms are $(0,0,0.4064)$ and $(0,0,0.5936)$, respectively.

IR	BV	Ni(1) atom $[m_a, m_b, m_c]$	Ni(2) atom $[m_a, m_b, m_c]$	Model	R_{mag}
Γ_1	$\boldsymbol{\psi}_1$	$[2,0,0]$	$[2,0,0]$	(i)	19.6
Γ_2	$\boldsymbol{\psi}_2$	$[1,2,0]$	$[-1,-2,0]$	(ii)	26.9
	$\boldsymbol{\psi}_3$	$[0,0,2]$	$[0,0,-2]$		
Γ_3	$\boldsymbol{\psi}_4$	$[1,2,0]$	$[1,2,0]$	(iii)	14.6
	$\boldsymbol{\psi}_5$	$[0,0,2]$	$[0,0,2]$		
Γ_4	$\boldsymbol{\psi}_6$	$[2,0,0]$	$[-2,0,0]$	(iv)	49.2

TABLE VI. Irreducible representations, and corresponding basis vectors for the space group $P\bar{3}m$ with $\boldsymbol{k}_{\mathrm{mag}} = (1/3,1/3,1/2)$. The coordinate of the Ni atom is $(0,0,0.5)$.

IR	BV	Ni atom $[m_a, m_b, m_c]$
Γ_1	$\boldsymbol{\psi}_1$	$[0,0,1]$
Γ_2	$\boldsymbol{\psi}_2$	$[1.5 - i\sqrt{3}/2, -i\sqrt{3}, 0]$
	$\boldsymbol{\psi}_3$	$[i\sqrt{3}, 1.5 + i\sqrt{3}/2, 0]$

ions for $\mathrm{Ba_3NiTa_2O_9}$ leads to two irreducible representations listed in Table VI. We safely assume that the magnitude of the magnetic moments on the $\mathrm{Ni^{2+}}$ ions are all the same because these ions are equivalent in the crystal structure. This assumption excludes the possibility of an irreducible representation Γ_1, from which the sinusoidal magnetic order is expected. In the irreducible representation Γ_2, there are two basis vectors $\boldsymbol{\psi}_2$ and $\boldsymbol{\psi}_3$ corresponding to the 120° structure with different chiralities. Figure 4(b) shows the neutron diffraction pattern at 1.5 K. The fitting curve is obtained by assuming the magnetic structure led from $\boldsymbol{\psi}_2$, which is shown in Figs. 4(c) and 4(d). The magnetic peaks

are well reproduced. The ordered moment of the $\mathrm{Ni^{2+}}$ ion is evaluated to be $1.86(6)\mu_{\mathrm{B}}$, which is consistent with that expected from the spin state of the $\mathrm{Ni^{2+}}$ ion $(S = 1, g = 2)$. The obtained profile factors $(R_{\mathrm{wp}} = 10.7\%, R_{\mathrm{e}} = 2.26\%)$ are comparable with those at 15 K. The determined magnetic structures and obtained ordered moments of the $\mathrm{Ni^{2+}}$ ion for $\mathrm{Ba_3NiTa_2O_9}$ are the same as those for the isostructural oxide $\mathrm{Ba_3NiNb_2O_9}$ [4]. The unidentified small peaks at $2\theta = 30°$ and $39°$ in Fig. 4(b) are independent of the temperature, which means that their origin is a small amount of impurity.

IV. DISCUSSION

Here, let us discuss the origin of the magnetic structure of $\mathrm{Ba_3NiTa_2O_9}$ and $\mathrm{Ba_2NiTeO_6}$. The 120° structure of $\mathrm{Ba_3NiTa_2O_9}$ is typical for a quasi-two-dimensional triangular lattice antiferromagnet with Heisenberg spins. The superexchange interaction via the $\mathrm{Ni^{2+}}$-$\mathrm{O^{2-}}$-$\mathrm{O^{2-}}$-$\mathrm{O^{2-}}$-$\mathrm{Ni^{2+}}$ path represented by $J_2^{(\mathrm{Ta})}$ in Fig. 1(f) is expected to be antiferromagnetic from the Goodenough-Kanamori rules [23]. It supports collinear antiferromagnetic spin coupling between the nearest-neighbor layers. On the other hand, the collinear magnetic order of $\mathrm{Ba_2NiTeO_6}$ cannot be explained by the antiferromagnetic interaction $J_3^{(\mathrm{Te})}$ in the case of a Heisenberg spin. In fact, the unique frustration in $\mathrm{Ba_2NiTeO_6}$ leads to collinear order, which will be explained as follows. The two neighboring triangular lattices of $\mathrm{Ba_2NiTeO_6}$ are magnetically coupled by the magnetic interaction $J_1^{(\mathrm{Te})}$, as shown in Fig. 1(b), which forms a buckled honeycomb lattice, as shown in Fig. 1(d). The magnetic interaction $J_3^{(\mathrm{Te})}$ can be regarded as the next-nearest-neighbor interaction in the honeycomb lattice, as shown in Fig. 1(d). Since the bond length of $J_1^{(\mathrm{Te})}$ is close to that of $J_3^{(\mathrm{Te})}$ owing to the buckled shape of the honeycomb lattice, the $J_1^{(\mathrm{Te})}$ and $J_3^{(\mathrm{Te})}$, which have $\mathrm{Ni^{2+}}$-$\mathrm{O^{2-}}$-$\mathrm{O^{2-}}$-$\mathrm{Ni^{2+}}$ paths, are comparative, and magnetic frustration is induced. The frustrated honeycomb lattices are coupled by the interaction $J_2^{(\mathrm{Te})}$, as shown in Fig. 1(b). $\mathrm{Ba_2NiTeO_6}$ is thus a rare experimental realization of a frustrated honeycomb lattice. We will consider the ground state of $\mathrm{Ba_2NiTeO_6}$ based on the classical Heisenberg model having easy-axis anisotropy. We will see that magnetic frustration and easy-axis anisotropy are the keys for the appearance of nontrivial collinear order.

We consider the following classical Hamiltonian,

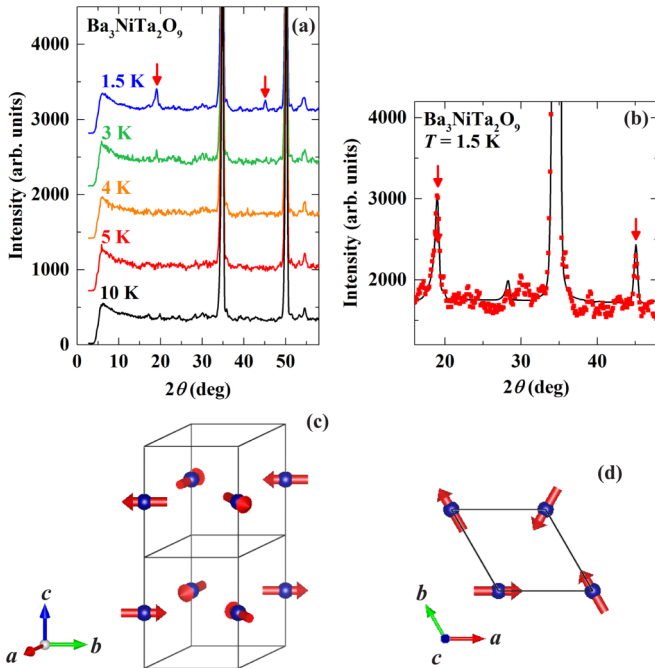$$H = \sum_{i,j} J_{i,j}^{(\mathrm{Te})} \boldsymbol{S}_i \cdot \boldsymbol{S}_j - D \sum_i S_{i,z}^2, \qquad (1)$$

FIG. 4. (a) Neutron diffraction patterns for $\mathrm{Ba_3NiTa_2O_9}$ at 1.5, 3, 4, 5, and 10 K. Data for different temperatures are scaled and vertically offset. The arrows show the magnetic peaks. (b) Neutron diffraction pattern for $\mathrm{Ba_3NiTa_2O_9}$ at 1.5 K. The arrows show the magnetic peaks. The solid squares and solid curve show the obtained and calculated data, respectively. (c) Determined magnetic structure of $\mathrm{Ba_3NiTa_2O_9}$. (d) Arrangement of spins for $\mathrm{Ni^{2+}}$ ions in the triangular lattice.

where S_i and $S_{i,z}$ represent the vectors for the spin of Ni^{2+} ion at the position of r_i and its component along the c axis, respectively. We take the sum in the first term of Eq. (1) for all the pairing of spins corresponding to $J_1^{(Te)}$, $J_2^{(Te)}$, and $J_3^{(Te)}$ in unit cells having the number of N. Here, we consider the ground-state phase diagram under the condition that the ground state has a coplanar magnetic structure with a single propagation vector q defined as

$$q = q_a \boldsymbol{a^*} + q_b \boldsymbol{b^*} + q_c \boldsymbol{c^*}. \qquad (2)$$

Let us define the vectors for the spins of Ni(k) ($k = 1,2$) in Table VI as $S_{i,k}$. Then it is written that

$$S_{i,k} = \mathrm{S}\{z \cos(q \cdot r_i + \alpha_k) + p \sin(q \cdot r_i + \alpha_k)\}. \qquad (3)$$

S, p, z, and α_k represent the length of the vector S, two orthogonal unit vectors, and arbitrary angle, respectively. Here, we set the vector z to be parallel to the crystallographic c axis. We introduce the constant $\alpha = \alpha_1 - \alpha_2$. Then, the energy of the state E obtained from the Hamiltonian in Eq. (1) is written as

$$
\begin{aligned}
\frac{E}{NS^2} = 3J_1^{(Te)} &\bigg[\cos\left\{ 2\pi\left(\frac{2}{3}q_a + \frac{1}{3}q_b + \frac{1}{3}q_c \right) - \alpha \right\} \\
&+ \cos\left\{ 2\pi\left(-\frac{1}{3}q_a + \frac{1}{3}q_b + \frac{1}{3}q_c \right) - \alpha \right\} \\
&+ \cos\left\{ 2\pi\left(-\frac{1}{3}q_a - \frac{2}{3}q_b + \frac{1}{3}q_c \right) - \alpha \right\} \bigg] \\
&+ 3J_2^{(Te)} \cos\alpha \\
&+ 6J_3^{(Te)} [\cos 2\pi q_a + \cos 2\pi q_b + \cos 2\pi(q_a + q_b)] \\
&- \frac{D}{N} \sum_{i,k} \cos^2(q \cdot r_i + \alpha_k).
\end{aligned}
\qquad (4)
$$

Let us evaluate q and α giving the lowest E. For q_c and α giving the minimum of E, the equations

$$
\begin{aligned}
\frac{\partial}{\partial q_c}\left(\frac{E}{NS^2} \right) = -2\pi J_1^{(Te)} &\bigg[\sin\left\{ 2\pi\left(\frac{2}{3}q_a + \frac{1}{3}q_b + \frac{1}{3}q_c \right) - \alpha \right\} \\
&+ \sin\left\{ 2\pi\left(-\frac{1}{3}q_a + \frac{1}{3}q_b + \frac{1}{3}q_c \right) - \alpha \right\} \\
&+ \sin\left\{ 2\pi\left(-\frac{1}{3}q_a - \frac{2}{3}q_b + \frac{1}{3}q_c \right) - \alpha \right\} \bigg] \\
&= 0
\end{aligned}
\qquad (5)
$$

and

$$
\begin{aligned}
\frac{\partial}{\partial \alpha}\left(\frac{E}{NS^2} \right) = 3J_1^{(Te)} &\bigg[\sin\left\{ 2\pi\left(\frac{2}{3}q_a + \frac{1}{3}q_b + \frac{1}{3}q_c \right) - \alpha \right\} \\
&+ \sin\left\{ 2\pi\left(-\frac{1}{3}q_a + \frac{1}{3}q_b + \frac{1}{3}q_c \right) - \alpha \right\} \\
&+ \sin\left\{ 2\pi\left(-\frac{1}{3}q_a - \frac{2}{3}q_b + \frac{1}{3}q_c \right) - \alpha \right\} \bigg] \\
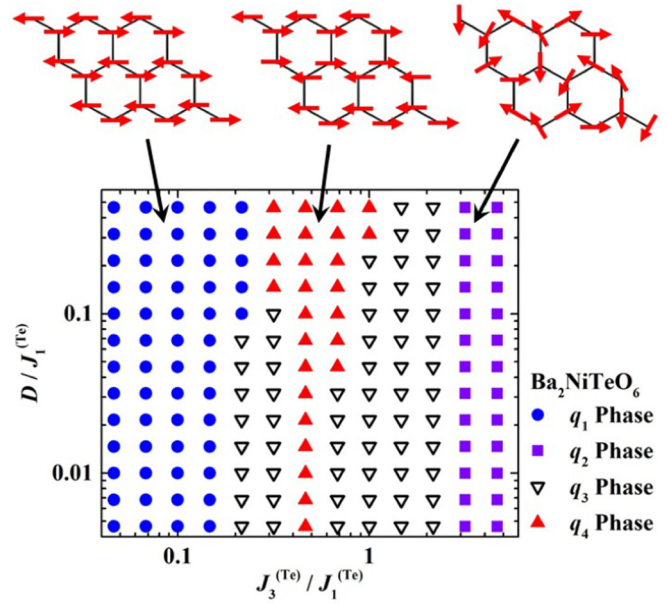&- 3J_2^{(Te)} \sin\alpha = 0
\end{aligned}
\qquad (6)
$$

FIG. 5. Magnetic phase diagram for the classical ground state obtained from the Hamiltonian in Eq. (1). The q_1, q_2, and q_4 phases are sketched above the phase diagram. The q_3 phase is incommensurate (not sketched). The q_4 phase corresponds to the experimental magnetic structure. The details of the q_1, q_2, q_3, and q_4 phases are shown in the main text.

are required. The first term of Eq. (6) is 0 because of Eq. (5). Then, Eq. (6) is rewritten as

$$\sin\alpha = 0. \qquad (7)$$

We can thus conclude that the lowest energy is obtained when $\alpha = 0$ or π. Here, we consider the case of $J_2^{(Te)} < 0$ and $\alpha = 0$ for reproducing the magnetic structure of Ba_2NiTeO_6. The q_{min} giving the lowest E is independent of $J_2^{(Te)}$ because the second term of Eq. (4) is not dependent on q. In order to obtain the q_{min} at a given D and $J_3^{(Te)}$, we calculated E for q in the reciprocal lattice space for $0 \leqslant q_a \leqslant 2$, $0 \leqslant q_b \leqslant 2$, and $0 \leqslant q_c \leqslant 3$ at intervals of $1/18$, $1/18$, and $1/12$, respectively. In the calculation, we set $J_1^{(Te)} = 1$ and $J_3^{(Te)} > 0$. We should note that the obtained ground states have threefold degeneracy because the Hamiltonian (1) keeps the three-rotation symmetry of the lattice.

The calculated phase diagram is shown in Fig. 5. When the first-neighbor interaction $J_1^{(Te)}$ is dominant, the Néel order where the energy fully gains the interaction $J_1^{(Te)}$ occurs with a propagation vector of $q_1 = (0,1,0.5)$. We refer to the phase as the q_1 phase. When the interaction $J_3^{(Te)}$ is dominant, the $120°$ structure with a propagation vector of $q_2 = (2/3,5/3,l)$ is stabilized because the system can be described as a conventional triangular lattice antiferromagnet. We refer to the phase as the q_2 phase. The value of l is arbitrary because the energy of the q_2 phase in fact is not dependent on l. In the intermediate region, an incommensurate magnetic order with a propagation vector of q_3 is obtained. We refer to the phase as the q_3 phase. At $J_3^{(Te)} \approx 0.5 J_1^{(Te)}$, we obtain a collinear antiferromagnetic order with a propagation vector of $q_4 = (0,3/2,0)$. We refer to the phase as the q_4 phase.

The collinear order of the q_4 phase where the energy partially gains $J_1^{(Te)}$ and $J_3^{(Te)}$ is different from that of the q_1 phase, as shown in Fig. 5. The collinear order of the q_1 and q_4 phases is more stabilized with increasing easy-axis anisotropy D. We emphasize that the experimentally determined collinear structure results from the magnetic frustration induced by the next-nearest-neighbor antiferromagnetic interaction in the honeycomb lattice. The phase diagram at $D \to 0$ resembles the classical phase diagram for the honeycomb lattice with antiferromagnetic nearest- and next-nearest-neighbor interactions [24]. In fact, the collinear order corresponding to that of the q_1 phase appears in the honeycomb lattice antiferromagnet Li_2MnO_3 [25]. In the honeycomb lattice, the collinear order corresponding to that of the q_4 phase is only stable at the boundary between two spiral order phases [24]. According to the phase diagram in Fig. 5, the interaction $J_3^{(Te)}$ that is comparative with interaction $J_1^{(Te)}$ is required in order to realize the q_4 phase. This requirement can be more easily achieved in the buckled honeycomb lattice shown in Fig. 1(d) than in the conventional honeycomb lattice as discussed above. In fact, $Fe_2Ga_2S_5$ exhibits a similar buckled honeycomb lattice [26], but a study on its magnetic structure has not yet been reported.

Finally, we focus on the region at $J_3^{(Te)} \approx J_1^{(Te)}$. The minimum value of D for stabilizing the collinear order increases with increasing $J_3^{(Te)}$ above $J_3^{(Te)} > 0.5 J_1^{(Te)}$, and it amounts to $0.3 J_1^{(Te)}$ at $J_3^{(Te)} = J_1^{(Te)}$. The requirement $D \geqslant 0.3 J_1^{(Te)}$ may be achieved in transition-metal oxides even if magnetic ions have no orbital degrees of the freedom. For example, the ratio of easy-axis anisotropy to the first-neighboring interaction for $Rb_4Mn(MoO_4)_3$ is estimated to be 0.22 [3]. Further investigations by inelastic neutron scattering are needed for quantitative analyses, which are in progress.

V. SUMMARY

We investigate the magnetic order of the buckled honeycomb lattice antiferromagnet Ba_2NiTeO_6 and quasi-two-dimensional triangular lattice antiferromagnet $Ba_3NiTa_2O_9$ by using neutron diffraction measurements. We observed the magnetic peaks for these oxides below transition temperatures. The magnetic structures are identified as a collinear magnetic order for Ba_2NiTeO_6 and a 120° structure for $Ba_3NiTa_2O_9$. We found that Ba_2NiTeO_6 is a rare experimental realization of the frustrated buckled honeycomb antiferromagnet. We consider the classical Heisenberg model with easy-axis anisotropy in order to discuss the magnetic frustration and single-ion anisotropy for Ba_2NiTeO_6. We reproduce the experimentally determined magnetic structure both in the case of $J_3^{(Te)} \approx 0.5 J_1^{(Te)}$ even for very small D and in the relatively wide range of $J_3^{(Te)} \approx 0.3 J_1^{(Te)} - J_1^{(Te)}$ for $D = 0.3 J_1^{(Te)}$. These results suggest that the collinear magnetic order of Ba_2NiTeO_6 is induced by magnetic frustration and easy-axis anisotropy.

[1] P. W. Anderson, Mater. Res. Bull. **8**, 153 (1973).

[2] H. Kadowaki, H. Takei, and K. Motoya, J. Phys.: Condens. Matter **7**, 6869 (1995).

[3] R. Ishii, S. Tanaka, K. Onuma, Y. Nambu, M. Tokunaga, T. Sakakibara, N. Kawashima, Y. Maeno, C. Broholm, D. P. Gautreaux, J. Y. Chan, and S. Nakatsuji, Europhys. Lett. **94**, 17001 (2011).

[4] J. Hwang, E. S. Choi, F. Ye, C. R. Dela Cruz, Y. Xin, H. D. Zhou, and P. Schlottmann, Phys. Rev. Lett. **109**, 257205 (2012).

[5] J. L. Soubeyroux, D. Fruchart, C. Delmas, and G. L. Flem, J. Magn. Magn. Mater. **14**, 159 (1979).

[6] M. F. Collins and O. A. Petrenko, Can. J. Phys. **75**, 605 (1997).

[7] M. Mekata and K. Adachi, J. Phys. Soc. Jpn. **44**, 806 (1978).

[8] S. Mitsuda, N. Kasahara, T. Uno, and M. Mase, J. Phys. Soc. Jpn. **67**, 4026 (1998).

[9] H. Nozaki, M. Månsson, B. Roessli, V. Pomjakushin, K. Kamazawa, Y. Ikedo, H. E. Fischer, T. C. Hansen, H. Yoshida, Z. Hiroi, and J. Sugiyama, J. Phys.: Condens. Matter **25**, 286005 (2013).

[10] S. Yamashita, Y. Nakazawa, M. Oguni, Y. Oshima, H. Nojiri, Y. Shimizu, K. Miyagawa, and K. Kanoda, Nat. Phys. **4**, 459 (2008).

[11] J. P. Sheckelton, J. R. Neilson, D. G. Soltan, and T. M. McQueen, Nat. Mater. **11**, 493 (2012).

[12] P. Köhl, U. Müller, and D. Reinen, Z. Anorg. Allg. Chem. **392**, 124 (1972).

[13] M. T. Weller and S. J. Skinner, Acta Crystallogr., Sect. C **55**, 154 (1999).

[14] M. Uchida, H. Tanaka, M. I. Bartashevich, and T. Goto, J. Phys. Soc. Jpn. **70**, 1790 (2001).

[15] M. B. Stone, M. D. Lumsden, S. Chang, E. C. Samulon, C. D. Batista, and I. R. Fisher, Phys. Rev. Lett. **100**, 237201 (2008).

[16] See Supplemental Material at http://link.aps.org/supplemental/10.1103/PhysRevB.93.024412 for the experimental data of the magnetic susceptibility and heat capacity for Ba_2NiTeO_6.

[17] M. W. Lufaso, Chem. Mater. **16**, 2148 (2004).

[18] T. Ono *et al.* (unpublished).

[19] J. Rodriguez-Carvajal, Physica B **192**, 55 (1993).

[20] A. Wills, Physica B **276-278**, 680 (2000).

[21] K. Momma and F. Izumi, J. Appl. Crystallogr. **44**, 1272 (2011).

[22] R. D. Shannon, Acta Crystallogr., Sect. A **32**, 751 (1976).

[23] J. Kanamori, J. Phys. Chem. Solids **10**, 87 (1959).

[24] J. Oitmaa and R. R. P. Singh, Phys. Rev. B **84**, 094424 (2011).

[25] S. Lee, S. Choi, J. Kim, H. Sim, C. Won, S. Lee, S. A. Kim, N. Hur, and J.-G. Park, J. Phys.: Condens. Matter **24**, 456004 (2012).

[26] S. Nakatsuji, H. Tonomura, K. Onuma, Y. Nambu, O. Sakai, Y. Maeno, R. T. Macaluso, and J. Y. Chan, Phys. Rev. Lett. **99**, 157203 (2007).